1996ApJ...470.1001M

THE ASTROPHYSICAL JOURNAL, 470:1001–1014, 1996 October 20
© 1996. The American Astronomical Society. All rights reserved. Printed in U.S.A.

THE DISPERSING CLOUD CORE AROUND T TAURI[1]

MUNETAKE MOMOSE,[2,3] NAGAYOSHI OHASHI,[4] RYOHEI KAWABE,[5]
MASAHIKO HAYASHI,[6] AND TAKENORI NAKANO[5]

Received 1996 February 21; accepted 1996 May 6

ABSTRACT

We have made ^{13}CO ($J = 1$–0) observations of T Tauri with the Nobeyama Millimeter Array (NMA) and with the Nobeyama 45 m telescope. The ^{13}CO ($J = 1$–0) emission detected with the NMA shows three different features: (1) a pair of ringlike features surrounding T Tauri with a radius of 30″ (corresponding to 4200 AU at the distance of 140 pc to T Tauri) at the velocities blueshifted and redshifted by less than 1 km s^{-1} from the systemic velocity, (2) a blueshifted compact feature 3″ east of T Tauri, and (3) another compact feature 7″ southwest of T Tauri at velocities redshifted by more than 1 km s^{-1}. On the other hand, the ^{13}CO maps obtained with the 45 m telescope show a smoothly extended feature near the systemic velocity, which is missed in the NMA observations, as well as the above-mentioned three features. The total masses of gas detected with the NMA and the 45 m telescope are estimated to be (0.054–0.23) $M_\odot$ and (0.31–1.3) $M_\odot$, respectively. The difference in the estimated mass between the two observations is mainly due to resolving out of the smoothly extended feature in the NMA observations.

The ^{13}CO rings are interpreted as biconical outflowing shells in a nearly pole-on configuration. The high-velocity stellar wind ejected from T Tauri is estimated to be energetic enough to drive these outflowing shells. We have analyzed the three-dimensional structure of the shells by correcting for the projection effect on the plane of the sky, and we have found that the spatial extent of the shells is nearly equal to or slightly smaller than the typical size of the molecular cloud cores in the Taurus Molecular Cloud. This fact indicates that the outflowing shells are part of the parent cloud core that still remains around T Tauri, which is now dispersing under the influence of the stellar wind. Such an environment around T Tauri is quite different from those around typical T Tauri stars, which are associated only with compact gaseous components. These results suggest strongly that T Tauri is one of the objects in the transitional phase from the protostar stage, in which a central star is deeply embedded in an infalling envelope, to the T Tauri stage, in which a central star is surrounded by a compact circumstellar disk instead of a spatially extended envelope.

Subject headings: circumstellar matter — ISM: jets and outflows — ISM: molecules — stars: individual (T Tauri) — stars: pre–main-sequence

1. INTRODUCTION

Understanding of the physical properties of young stellar objects has been greatly improved by the analysis of their spectral energy distributions (SEDs). Lada (1987) (see also Lada & Wilking 1984) proposed that young stellar objects can be divided into three classes by their spectral indices α_{IR}, which is the mean value of $d(\log \lambda F_\lambda)/d(\log \lambda)$ in the wavelength range between $\lambda = 1$ μm and 10 μm: class I with $\alpha_{IR} > 0$, class II with $-2 < \alpha_{IR} \leq 0$, and class III with $-3 < \alpha_{IR} \leq -2$. Class I sources are often found at the centers of ammonia cores without optical counterparts in the Palomar Observatory Sky Survey prints (Myers et al. 1987; see also Beichman et al. 1986). Theoretical models have shown that SEDs of class I sources can be reproduced by the emission from mass-accreting protostars (Adams & Shu 1986; Kenyon, Calvet, & Hartmann 1993). On the other hand, class II sources correspond to optically visible T Tauri stars. SEDs of many class II objects can be well explained with a system composed of a central star and a circumstellar disk (Kenyon & Hartmann 1987; Adams, Lada, & Shu 1987; Bertout, Basri, & Bouvier 1988; Miyake & Nakagawa 1995). On the basis of these studies, it is widely accepted that the SED classes introduced by Lada (1987) correspond to different evolutionary stages of young stellar objects (e.g., Adams et al. 1987).

In the course of evolution from class I (optically invisible) to class II (optically visible) sources, dissipation of the parent cloud cores should occur, probably due to mass accretion onto the central star-disk systems and/or due to dispersal produced by the outflow (e.g., Hayashi et al. 1994; Ohashi et al. 1991, 1996). To gain a better understanding of the evolution processes from protostars to typical T Tauri stars, we have to investigate in detail the objects that are in a "transitional phase" between these two evolutionary stages. Some T Tauri stars with so-called flat spectrum are good candidates for such objects. They exhibit very flat SEDs in the whole range of infrared wavelengths ($\lambda = 1$–100 μm) and luminosities with huge infrared excesses, which are significantly larger than the "stellar" luminosities. It is difficult to explain their SEDs with a central star plus disk model unless these T Tauri stars have active disks with an

[1] Based on the observations made at the Nobeyama Radio Observatory (NRO), which is a branch of the National Astronomical Observatory, an inter-university research institute operated by the Ministry of Education, Science, Sports, and Culture.

[2] Department of Astronomical Science, The Graduate University for Advanced Studies, Nobeyama Radio Observatory, Nobeyama, Minamimaki, Minamisaku, Nagano 384-13, Japan.

[3] momose@nro.nao.ac.jp.

[4] Harvard-Smithsonian Center for Astrophysics, MS78, 60 Garden Street, Cambridge, MA 02138.

[5] Nobeyama Radio Observatory, Nobeyama, Minamimaki, Minamisaku, Nagano 384-13, Japan.

[6] SUBARU Project Office, National Astronomical Observatory, Mitaka, Tokyo 181, Japan.

© American Astronomical Society • Provided by the NASA Astrophysics Data System

1996ApJ...470.1001M

unorthodox radial temperature distribution, $T(r) \propto r^{-0.5}$(Adams, Lada, & Shu 1988). Recently, Calvet et al. (1994, hereafter CHKW) have proposed an attractive explanation for the flat SEDs; the SEDs of two flat-spectrum T Tauri stars, HL Tauri and T Tauri, can be reproduced by introducing tenuous axisymmetric infalling envelopes which surround the central star-disk systems (see also Kenyon et al. 1993). Recent observational results also show that HL Tauri is accompanied by a spatially extended envelope, suggesting that it is younger than typical T Tauri stars. Aperture synthesis ^{13}CO ($J = 1$–0) observations of HL Tauri with the Nobeyama Millimeter Array (NMA) have shown that the kinematics of the disklike structure around HL Tauri with a radius of 1400 AU is dominated by infalling motion (Hayashi, Ohashi, & Miyama 1993). This suggests that HL Tauri is significantly younger than typical T Tauri stars in the sense that dynamical mass accretion onto the central star-disk system is still going on. Observations of HL Tauri with the *Hubble Space Telescope* (Stapelfeldt et al. 1995) have shown that there is no stellar component in the HL Tauri region at optical wavelengths, indicating that the central star is still deeply embedded in circumstellar material. It will be important to investigate physical properties of the other T Tauri stars with flat SEDs as well in order to clarify whether they are in the "transitional phase" from protostars to typical T Tauri stars.

T Tauri shows a typical flat SED (Adams et al. 1988; CHKW). It is well known tht T Tauri is a rare example of visible T Tauri stars with a bipolar molecular outflow (Edwards & Snell 1982). T Tauri is a binary system, consisting of the main star T Tau(N) and an IR companion T Tau(S) with a linear separation of 0.″6 (Dyck, Simon, & Zuckerman 1982). Near-infrared polarization images around T Tauri indicated that T Tauri is surrounded by a nonspherical dusty envelope with a spatial extent exceeding 10^3 AU (Weintraub et al. 1992; Whitney & Hartmann 1993). High-resolution interferometric observations with ^{12}CO ($J = 1$–0) have revealed the presence of a gaseous structure extending $\sim 10''$ around T Tauri (Weintraub, Masson, & Zuckerman 1989, hereafter WMZ). WMZ argued that the velocity field of the ^{12}CO ($J = 1$–0) emission could be explained by a disk in Keplerian rotation around T Tauri.

In this paper, we report the results of aperture synthesis ^{13}CO ($J = 1$–0) observations of T Tauri by using the Nobeyama Millimeter Array (NMA) and the results of ^{13}CO ($J = 1$–0) mapping observations around T Tauri with the Nobeyama 45 m telescope. In § 2 we describe the observational parameters. We present the results of these observations in § 3. In § 4.1 we discuss the origin of the ^{13}CO emission. In § 4.2 we investigate the driving mechanism and three dimensional structure of the shells, and in § 4.3, we discuss the physical nature of the shells and the evolutionary status of T Tauri.

2. OBSERVATIONS

2.1. ^{13}CO ($J = 1$–0) *Observations with the Nobeyama Millimeter Array*

Aperture synthesis ^{13}CO ($J = 1$–0) observations were made during a period from 1993 November to 1994 March with the NMA, which was composed of five 10 m dishes. We used the SIS receivers (Sunada, Kawabe, & Inatani 1993) whose system noise temperatures were typically 400 K (double sideband [DSB]) at the zenith. We employed the digital FFT spectral correlator FX (Chikada et al. 1987), which gave a frequency resolution of 156 kHz, corresponding to the velocity resolution of 0.425 km s^{-1}. The 110 GHz continuum emission from T Tauri was observed simultaneously with a bandwidth of 160 MHz. The phase and gain of the array system were calibrated by observing 0420−014 or 0528+134 every 30 minutes. The flux density of 0420−014 at 110 GHz was 2.3 Jy in 1993 November, and that of 0528+134 was 4.83 Jy at 110 GHz from February to March in 1994.

We made the observations for two fields of view; the first field is centered on the position of T Tauri [R.A. (1950) = $4^h19^m04^s.21$, decl. (1950) = +19°25′05″.4: Herbig & Bell 1988], and the second is on the position 37″.4 southwest (P.A. = 232°) of T Tauri. Two compact array configurations (giving 20 baselines) were used for the observations of both fields. Before making ^{13}CO images of each field, the continuum level was subtracted from the visibility data. After the conventional deconvolution process (CLEAN) and the correction for the primary beam (FWHM = 65″) attenuation in each field, the ^{13}CO images of the two fields were mosaicked in such a way as to minimize noise in each combined channel map. The size of the synthesized beam is 7″.2 × 5″.5 (FWHM) with a P.A. of 140°. This corresponds to 1000 AU × 770 AU at the distance 140 pc of the Taurus Molecular Cloud (Elias 1978). The minimum baseline in the observations was 5 kλ, so that our observations are insensitive to structures with sizes greater than 41″, corresponding to $\sim$5800 AU. The rms noise level in the combined channel map is 115 mJy beam^{-1} at the center of the field of view and 354 mJy beam^{-1} at the edge of the field of view.

2.2. *Observations with the Nobeyama* 45 m *Telescope*

We made mapping observations of ^{13}CO ($J = 1$–0) on 1995 March 13 and 15 with the Nobeyama 45 m telescope. We used the SIS 2 × 2 focal plane array receiver (Sunada et al. 1995), which consists of four beams with almost identical half-power beamwidths of 17″ at 110 GHz. We employed acousto-optical spectrometers with a spectral resolution of 37 kHz, corresponding to the velocity resolution of 0.1 km s^{-1} at 110 GHz. The system noise temperature was typically 300 K (DSB) during our observations. Pointing of the telescope was checked once an hour by observing the SiO ($J = 1$–0) maser of NML Tau at 43 GHz. The pointing accuracy was better than 4″. We observed Orion KL with ^{13}CO ($J = 1$–0) once a day in order to calibrate the difference in gain among the four beams. We mapped a 119″ × 119″ area around T Tauri with two different grid spacings; 12″ spacings for the inner 102″ × 102″ area and 17″ spacings for the outer region. In § 3.2, we derive gas mass on the basis of T_R^*, which was introduced by Kutner & Ulich (1981). In converting the antenna temperature (T_A^*) to T_R^*, we assumed the forward scattering and spillover efficiency of the 45 m telescope to be 0.85.

3. RESULTS

Before showing our present results, we comment on the systemic velocity of T Tauri because it is an important parameter for understanding the results. Hartmann et al. (1986) have estimated the line-of-sight velocity of T Tauri to be $V_{\rm HEL} = +19.1 \pm 1.2$ km s^{-1} (corresponding to $V_{\rm LSR} = +8.2 \pm 1.2$ km s^{-1}) from spectroscopic observations of T

© American Astronomical Society • Provided by the NASA Astrophysics Data System

1996ApJ...470.1001M

Tauri at optical wavelengths. Recent CO observations toward T Tauri have shown that the peak velocities of the $J = 3$–2 and $J = 6$–5 lines are $V_{LSR} \approx +8$ km s^{-1} (Schuster et al. 1993). It is natural to regard the peak velocities of these higher CO transitions as the plausible systemic velocity of T Tauri because these lines originate in the warm and dense circumstellar material in the vicinity of T Tauri (Schuster et al. 1993). This systemic velocity estimated from the CO lines is consistent with that obtained by Hartmann et al. (1986). Based on these observational results, we assume the systemic velocity of T Tauri, V_{LSR}, to be +8.2 km s^{-1} unless otherwise specified.

3.1. ^{13}CO ($J = 1$–0) *Emission around T Tauri Obtained by the NMA Observations*

3.1.1. *Morphology and Velocity Field*

Figure 1 (Plate 25) shows the mosaicked velocity channel maps of the ^{13}CO emission around T Tauri obtained with the NMA. ^{13}CO emission above the 3 σ level was detected in the velocity range between $V_{LSR} = 5.85$ km s^{-1} and 9.67 km s^{-1}. The detected ^{13}CO emission can be characterized by the following three features: (1) spatially extended features that are found in the range between $V_{LSR} = 7.12$ km s^{-1} and 8.82 km s^{-1}, (2) a compact feature 3″ east of T Tauri in the range from 5.85 km s^{-1} to 7.97 km s^{-1}, and (3) a faint, compact feature 7″ southwest of T Tauri seen in the maps at $V_{LSR} = 9.25$ km s^{-1} and 9.67 km s^{-1}. In the following, we will describe morphology and velocity field of each feature in detail.

3.1.1.1. *The Spatially Extended Features*

We have found some difference in the distribution of the extended features between blueshifted and redshifted velocities. To make the overall structures of the blueshifted and redshifted extended features clearer, we made two maps integrated over the velocity ranges of $V_{LSR} = 7.12$–7.55 km s^{-1} and $V_{LSR} = 8.40$–8.82 km s^{-1} as shown in Figures 2*a* and 2*b*, respectively. The extended feature at blueshifted velocities (Fig. 2*a*) consists of two regions of the emission. One is a blob covering the northeast area from T Tauri with a size of 35″ × 25″. The blob contains several emission peaks. The other emitting region appears at ~35″ west of T Tauri and continues to the southwest of T Tauri with a width of ~20″. Although this region also contains several peaks, the one at 45″ southwest of T Tauri is most prominent. Similarly to the blueshifted feature, the extended feature at redshifted velocities (Fig. 2*b*) also consists of two emitting regions. One is located at ~30″ east of T Tauri with a size of 30″ × 15″. The other extends from ~25″ west to ~20″ south of T Tauri with several emission peaks that are connected mutually by diffuse emission.

We have identified two arcs in each extended feature by connecting the emission peaks as indicated by thick gray lines in Figures 2*a* or 2*b*. Hereafter we call the extended features "a pair of rings," though some parts of the rings seem to be missing (i.e., the southern part of the blueshifted ring and the northern part of the redshifted one). Both rings have a radius of ~30″, which corresponds to ~4200 AU at the distance to T Tauri. The central positions of the rings are different from each other; the center of the blue ring (Fig. 2*a*) is located at ~15″ southwest of T Tauri, but the red one (Fig. 2*b*) is almost centered at the stellar position. Figure 3, showing a position-velocity diagram along a line connecting the centers of the two rings (P.A. = 77°) together with the integrated ^{13}CO ($J = 1$–0) intensity map, demonstrates clearly the positional difference between the centers of the red ring (denoted A, B, and C) and the blue ring (denoted D, E, and F).

Comparing our ^{13}CO observations with other observational results, we have found some important character-

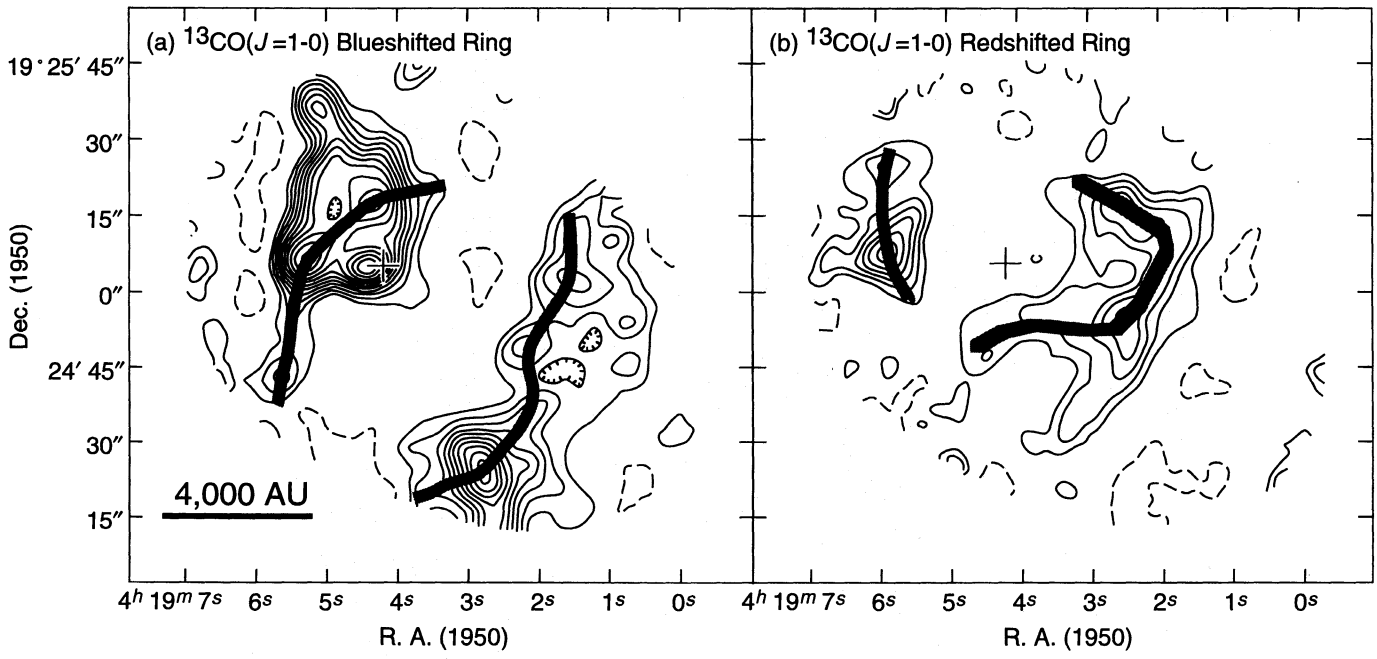

FIG. 2.—Spatially extended features of the ^{13}CO ($J = 1$–0) emission with the NMA observations: the maps integrated over the velocity range (*a*) $V_{LSR} = 7.12$–7.55 km s^{-1} and (*b*) $V_{LSR} = 8.40$–8.82 km s^{-1}. The systemic velocity is $V_{LSR} = 8.2$ km s^{-1}. The thick gray lines connecting several peaks of the emission show a pair of "^{13}CO rings." The cross in each panel indicates the position of T Tau(N). The contour spacing is 2 σ, starting at 3 σ (1 σ = 124 mJy beam^{-1}). Dashed lines are −3 σ contours.

© American Astronomical Society • Provided by the NASA Astrophysics Data System

1996ApJ...470.1001M

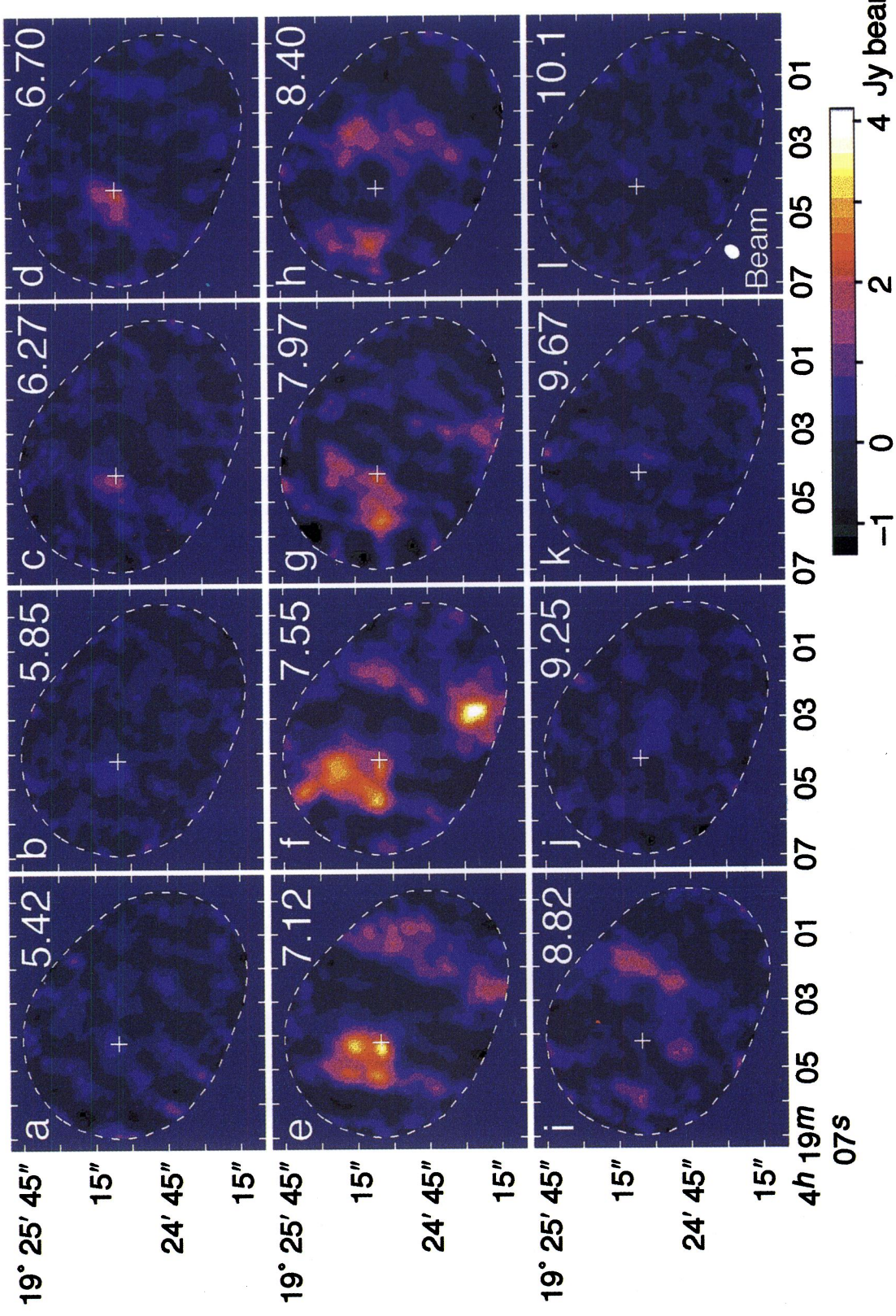

FIG. 1.—The pseudo color-velocity channel maps of the T Tauri region with the ^{13}CO ($J = 1–0$) line obtained by the NMA. The corresponding LSR velocity in km s^{-1} is noted in the upper right corner of each panel. The white dashed line indicates the field of view of our observations. The cross marks the position of T Tau(N) (Herbig & Bell 1988). It should be noted that the separation between T Tau(N) and the IR companion, T Tau(S), is so small (~0″.6, Dyck et al. 1982) that the positions of these two stars overlap each other in these channel maps.

© American Astronomical Society • Provided by the NASA Astrophysics Data System

1996ApJ...470.1001M

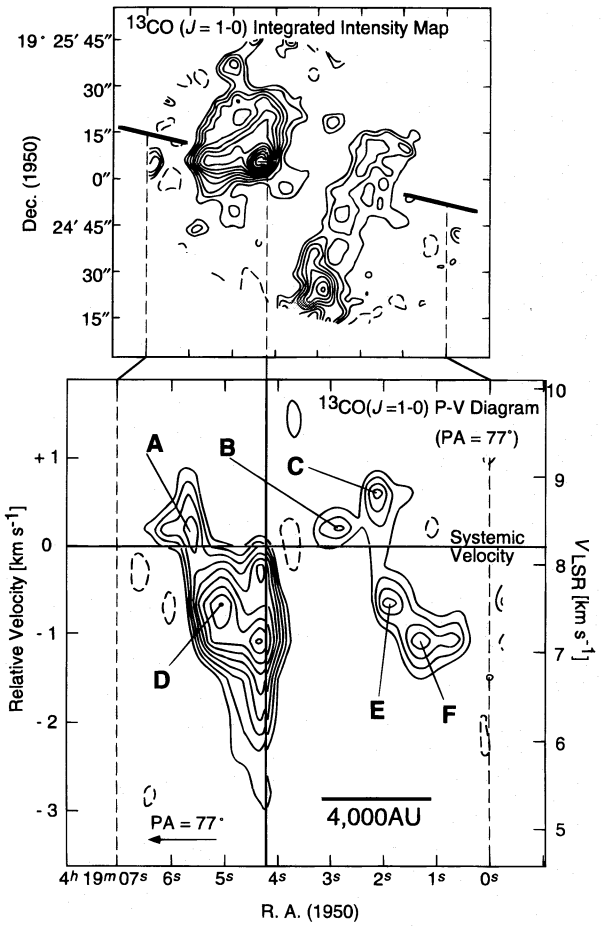

FIG. 3.—(*Top*) Integrated intensity map of the ^{13}CO (J = 1–0) emission. The contour spacing is 1.5 σ, starting at 3 σ (1 σ = 48.3 mJy beam^{-1}). Dashed lines are −3 σ contours. (Bottom) The position-velocity diagram cutting along the thick line (P.A. = 77°) in the upper panel. We adopt V_{LSR} = +8.2 km s^{-1} as the systemic velocity of T Tauri. The letters A, B, and C indicate the emission peaks contained in the redshifted rings, and the letters D, E, and F indicate those in the blueshifted rings, respectively. The contour spacing is 1.5 σ, starting at 3 σ (1 σ = 177 mJy beam^{-1}). Dashed lines are −3 σ contours.

istics, which can be clues to understanding the origin of these rings. Figures 4*a* and 4*b* (Plate 26) show our contour maps of the blueshifted ^{13}CO ring superposed on a K'-band image of the reflection nebula NGC 1555 (Hodapp 1994) and on an I-band coronagraphic image of T Tauri (Nakajima & Golimowski 1995), respectively. NGC 1555 clearly delineates the inner edge of the western arc of the blue ring (Fig. 4*a*). The reflection nebula in the vicinity of T Tauri is found to have similar curvature as the north-southeast arc of the blue ring (Fig. 4*b*). These results imply that the inner part of the blue ring is illuminated by the light from T Tauri. Figure 5 compares the ^{12}CO (J = 3–2) emission from the molecular outflow with moderately high velocities (blueshifted or redshifted by 2–13 km s^{-1} from the systemic velocity) (Schuster 1994; Schuster et al. 1996) with the ^{13}CO rings, showing that the strongest parts of the blueshifted and redshifted outflows are located inside the blue and red rings, respectively. This fact implies that the dense gas traced by the ^{13}CO (J = 1–0) emission with low velocities surrounds the moderately high velocity outflow. These characteristics of the ^{13}CO rings are understood naturally by assuming that the origin of the rings is a pair of shells outflowing with small velocities. We will discuss this point further in § 4.1.

3.1.1.2. *The Spatially Compact Features*

We have found a spatially compact feature ~3″ east of T Tauri in channel maps at all the blueshifted velocities V_{LSR} = 5.85–7.97 km s^{-1}. This features appears at V_{LSR} = 5.85 km s^{-1} (Fig. 1*b*), has a bright peak with faint and diffuse emission around it at V_{LSR} = 6.27 and 6.70 km s^{-1} (Figs. 1*c*–1*d*), and becomes most prominent in the velocity range of V_{LSR} = 7.12–7.97 km s^{-1} (Figs. 1*e*–1*g*). The size of this feature is 5″ × 5″ at V_{LSR} = 7.12 km s^{-1}. WMZ also detected this compact feature in the velocity range of V_{LSR} = 7.4–7.9 km s^{-1} with their ^{13}CO (J = 1–0) observations. The other compact feature at ~7″ southwest of T Tauri is found in the maps at V_{LSR} = 9.25 and 9.67 km s^{-1} (Figs. 1*j*–1*k*), with a size of 4″ × 10″.

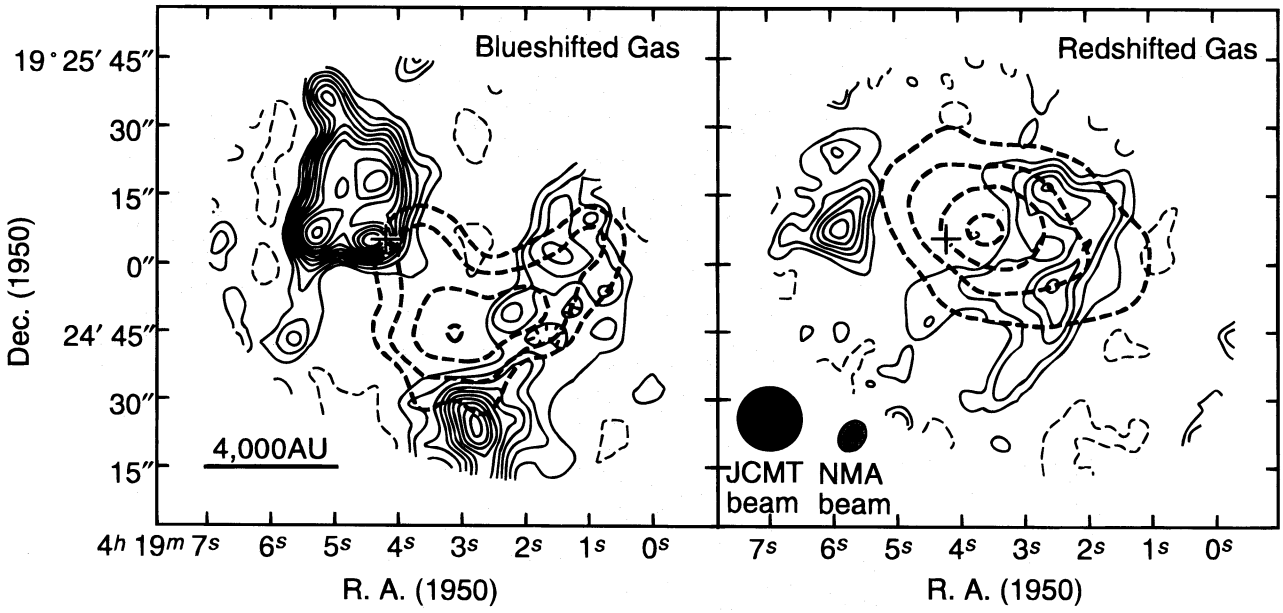

FIG. 5.—Maps of the ^{13}CO rings shown in Fig. 2 are superposed on the ^{12}CO (J = 3–2) maps drawn in dashed lines (Schuster 1994): *left*: The blueshifted ^{12}CO (J = 3–2) map integrated over V_{LSR} = −5 to +6 km s^{-1}; *right*: the redshifted ^{12}CO (J = 3–2) map integrated over V_{LSR} = +9 to +21 km s^{-1}.

© American Astronomical Society • Provided by the NASA Astrophysics Data System

1996ApJ...470.1001M

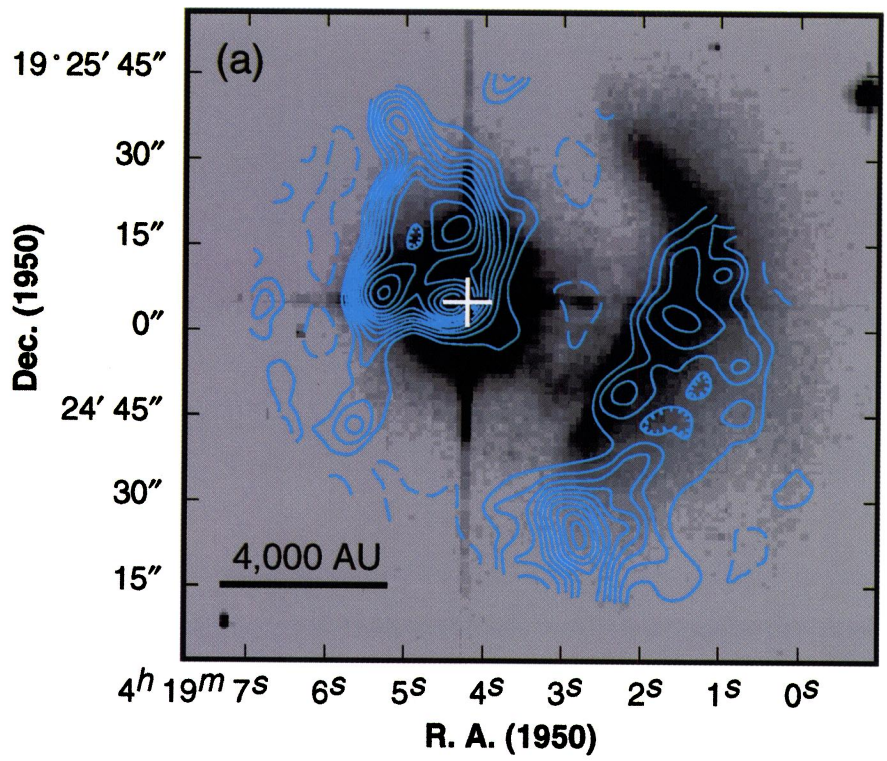

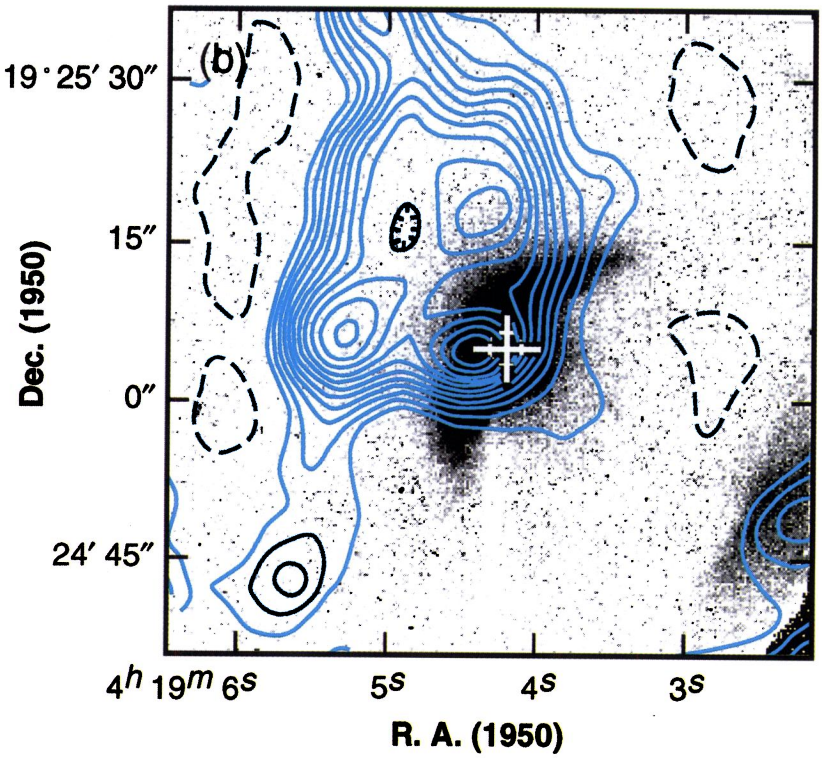

FIG. 4.—(*a*) Contour map of the blueshifted ^{13}CO ($J = 1–0$) ring superposed on a K'-band image of the reflection nebula NGC 1555 (Hodapp 1994). (*b*) Contour map of the blueshifted ^{13}CO ($J = 1–0$) ring superposed on an I-band coronagraphic image of T Tauri (Nakajima & Golimowski 1995).

MOMOSE et al. (see 470, 1004)

© American Astronomical Society • Provided by the NASA Astrophysics Data System

© American Astronomical Society • Provided by the NASA Astrophysics Data System

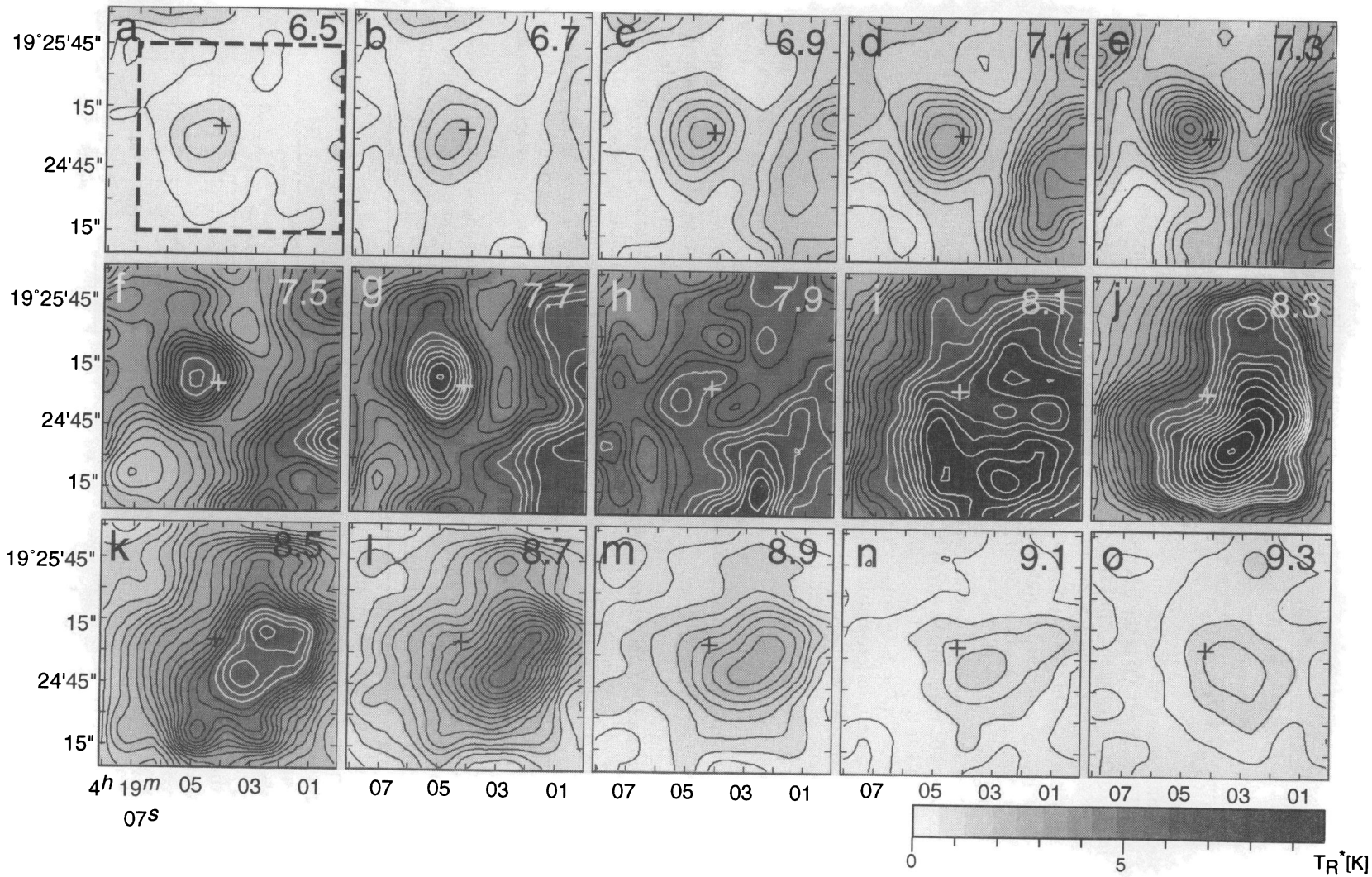

FIG. 6.—Velocity channel maps of the T Tauri region in the ^{13}CO ($J = 1$–0) line, obtained by the Nobeyama 45 m telescope. The corresponding LSR velocity in km s^{-1} is noted in the upper right corner of each panel. The cross indicates the position of T Tau(N). Contour spacing is 3 σ, starting at 3 σ (1 σ = 0.104 K in T_R^*). Contours above $T_R^* = 5.90$ K are shown in white lines.

1996ApJ...470.1001M

3.1.2. *Total Mass of the Observed Gas around T Tauri*

We can estimate the total mass of the molecular gas detected with the NMA by the following equation (Scoville et al. 1986):

$$M_{\rm gas} = 5.37 \times 10^{-5} T_{\rm ex} \exp\left(\frac{5.29}{T_{\rm ex}}\right) \frac{\tau_{^{13}\rm CO}}{[1 - \exp(-\tau_{^{13}\rm CO})]} \times \left(\frac{d}{140\ \rm pc}\right)^2 \left[\frac{10^{-6}}{X(^{13}\rm CO)}\right] \int S_v\, dv\, M_\odot\ , \quad (1)$$

where $T_{\rm ex}$ is the excitation temperature of ^{13}CO at the $J = 1$ level, d is the distance to T Tauri, $X(^{13}\rm CO)$ is the fractional abundance of ^{13}CO relative to H_2, $\tau_{^{13}\rm CO}$ is the optical depth of the gas for the ^{13}CO ($J = 1$–0) line, and $\int S_v\, dv$ is the integrated flux in units of Jy km s^{-1}. On the assumption of optically thin ^{13}CO emission ($\tau_{^{13}\rm CO} \ll 1$), the integrated flux of 118 Jy km s^{-1} gives us the total gas mass of (0.054–0.23) $M_\odot$ with $T_{\rm ex} = 10$–30 K and $X(^{13}\rm CO) = (1\text{–}2) \times 10^{-6}$. If $\tau_{^{13}\rm CO}$ were considerably greater than 1, the above estimate of the gas mass would be a lower limit. However, WMZ estimated $\tau_{^{13}\rm CO}$ to be at most 1.14 at $V_{\rm LSR} = 7.6$ km s^{-1} from the peak intensities of the ^{12}CO ($J = 1$–0) and ^{13}CO ($J = 1$–0) lines obtained with their interferometric observations. Therefore, it is unlikely that we have underestimated significantly the total mass of the observed gas by assuming that the ^{13}CO ($J = 1$–0) emission is optically thin. Note that spacially extended components were resolved out in the NMA observations, so that the total gas mass within the field of view of the NMA observations may be underestimated, as will be described in the next section.

3.2. ^{13}CO ($J = 1$–0) *Emission around T Tauri Obtained by the Nobeyama* 45 m *Telescope and Comparison with the Results of the NMA Observations*

Figure 6 shows channel maps of the ^{13}CO emission obtained by the 45 m telescope with a velocity resolution of 0.2 km s^{-1}. The resultant rms noise level is $T_R^* = 0.104$ K. The overall distributions of the ^{13}CO emission in Figure 6 are similar to those obtained with the NMA (Fig. 1). In the channel maps (Figs. 6*d*–6*g*) for $V_{\rm LSR} = 7.1$–7.7 km s^{-1}, we can find two prominent emission features: a peak located $\sim$20″ northeast of T Tauri, and a ridgelike feature starting at $\sim$50″ northwest of T Tauri and extending along the western edge of the channel maps. These two emission features are almost coincident with the blueshifted ring detected by the NMA observations (Fig. 2*a*). In the channel maps (Figs. 6*j*–6*l*) for $V_{\rm LSR} = 8.3$–8.7 km s^{-1}, the ^{13}CO emission has a strong peak to the southwest of T Tauri, with an arclike extended feature opened toward T Tauri at lower contour levels. This feature seems to correspond to the southwestern arc of the redshifted ring seen in the NMA map (see Fig. 2*b*). At higher blueshifted ($\leq$6.9 km s^{-1}; Figs. 6*a*–6*c*) and redshifted ($\geq$8.9 km s^{-1}; Figs. 6*n*–6*o*) velocities, spatially compact features can be seen at $\sim$5″ east and at $\sim$5″ southwest, respectively, of T Tauri, as was also seen in the NMA channel maps (see Figs. 1*b*–1*d* and 1*j*–1*k*). On the other hand, the ^{13}CO emission in the channel maps near the systemic velocity, Figures 6*h* and 6*i* for $V_{\rm LSR} = 7.9$–8.1 km s^{-1}, is distributed smoothly compared with the other channel maps in Figure. 6, and each emission peak coincides well with the corresponding peak in the NMA channel maps.

In order to calculate the total mass of the molecular gas from the 45 m observations, the flux density in the field of view of the NMA observations was estimated from the flux density in the dashed rectangular area (see Fig. 6*a*) by correcting the difference in the solid angles. A total flux of 679 Jy km s^{-1} has been obtained for the velocity range $V_{\rm LSR} =$ 5.8–9.6 km s^{-1}. With this flux, equation (1) gives the total gas mass of 0.31–1.3 $M_\odot$ under the same assumptions as for the NMA case. This is 5.8 times larger than the mass derived from the total flux obtained with the NMA.

The difference in the total flux and the estimated mass between the NMA and 45 m observations is mainly due to resolving out of the smoothly extended feature in the NMA observations. Figure 7 compares the total flux densities obtained with the NMA and with the 45 m telescope; the missing flux density at velocities blueshifted or redshifted by $>$0.5 km s^{-1} in the NMA observations is less than 75% of the 45 m flux density, while in the velocity range of $V_{\rm LSR} =$ 7.7–8.7 km s^{-1}, more than 80% of the 45 m flux density is missing in the NMA observations. It indicates that the smoothly extending feature is dominated near the systemic velocity, and this feature is not detected by the NMA observations.

3.3. *Continuum Emission Obtained by the NMA Observations*

We detected unresolved continuum emission toward T Tauri at 110 GHz with the NMA. The position of the continuum emission is coincident with that of T Tauri (Herbig & Bell 1988), and with our angular resolution we could not separate the contribution of the main star T Tau(N) from that of the IR companion T Tau(S), which locates 0.″6 south of the main star (Dyck et al. 1982). The total flux density of the continuum emission is 48 $\pm$ 7 mJy in the present observations. This is smaller than the previously obtained flux densities toward T Tauri, 75 mJy at 110 GHz (WMZ) and 56 $\pm$ 10 mJy at 98 GHz (Ohashi et al. 1996), even if we take into account a possible systematic error in the flux calibration ($\leq$10%).

A possible cause for the smaller flux density obtained by our observations is the time variability of nondust radiation which may contribute partly to the continuum emission at millimeter wavelengths. Recently, Skinner & Brown (1994)

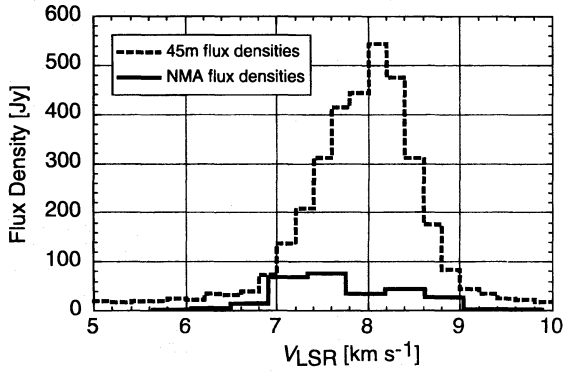

FIG. 7.—Comparison of the total flux densities obtained by the NMA (*solid line*) with those obtained by the 45 m telescope (*dashed line*). The total flux densities with the 45 m telescope were measured in the rectangular area indicated by the thick broken line in Fig. 6*a* and were corrected for the difference in the solid angles between the two observations.

© American Astronomical Society • Provided by the NASA Astrophysics Data System

1996ApJ...470.1001M

have analyzed high angular resolution images of T Tauri at centimeter wavelengths and have interpreted the centimeter emission from T Tau(N) as free-free emission and that from T Tau(S) as nonthermal gyrosyncrotron emission. The contribution of the gyrosynchrotron emission to the continuum at 110 GHz may be negligible because of its negative spectral index between 2 and 3.6 cm obtained by simultaneous total flux measurements (Skinner & Brown 1994). On the other hand, the free-free emission may contribute significantly to the continuum emission at 110 GHz and may show time variability. For example, according to the spherical constant-velocity wind model by Panagia & Felli (1975), the spectral index of the predicted free-free emission is positive ($\alpha = +0.6$, where $S_\nu \propto \nu^\alpha$), and the emission shows time variability due to the variation of mass-loss rate and/or that of ionization degree (see also Panagia 1991). In order to confirm this for T Tauri, we need further photometric studies of the continuum emission at millimeter-centimeter wavelengths.

4. DISCUSSION

4.1. *Origin of the* ^{13}CO *Emission*

To explain the ^{13}CO emission maps of T Tauri in a consistent manner, we propose a model of biconical outflowing shells in a nearly pole-on configuration as illustrated in Figure 8. In this model, we suppose that the axis of the outflowing shells is at an angle of about 10° with the line of sight and has a P.A. $\approx$ 257° (southwestward) on the sky on its near side. Herbst et al. (1986) estimated the angle between the line of sight and the rotation axis of T Tau(N) to be 8°–13° from its rotation period and projected rotation velocity. Moreover, the near-IR polarization image of T Tauri can be reproduced well by the scattered light from

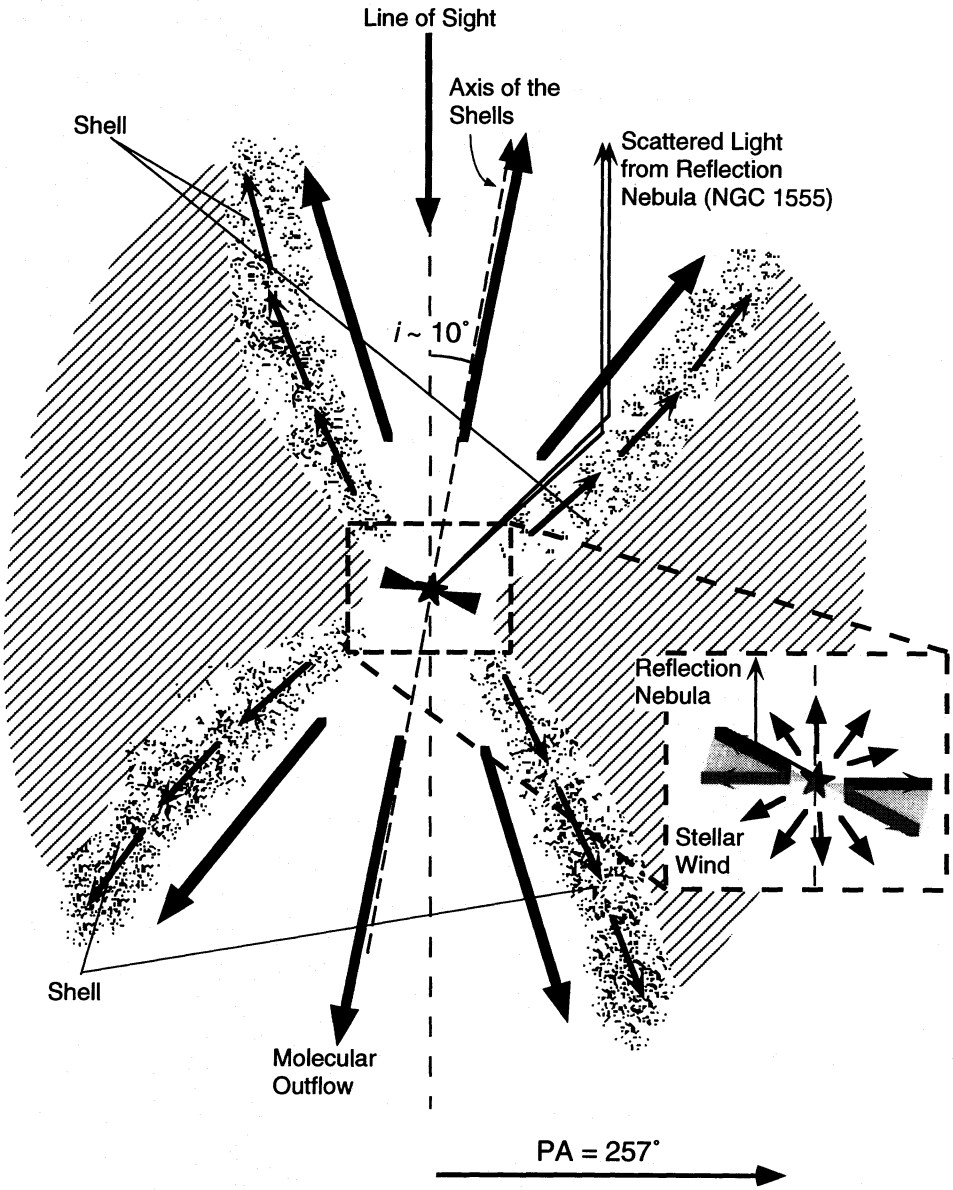

FIG. 8.—Schematic illustration of the biconical outflowing shell model. The shells, indicated by dots, are expected to be observed as the ^{13}CO rings. The reflection nebula NGC 1555 is interpreted as the inner surface of the nearer shell which scatters the stellar light. The origin of the spatially compact features near the star may be interpreted as the outflowing gas on the surface of the geometrically thick disk around T Tauri, indicated by the thick gray lines. A significant amount of the ambient gas is expected to exist around T Tauri, as indicated by the hatching.

© American Astronomical Society • Provided by the NASA Astrophysics Data System

1996ApJ...470.1001M

dust contained in an axisymmetric envelope with a pole-on configuration (Weintraub et al. 1992; Whitney & Hartmann 1993). The configuration and the shape of the biconical outflowing shell in our model are consistent with these estimates. The position angle on the sky of the shell axis in our model agrees roughly with that (270°) of the blueshifted jet ejected from T Tauri (Bührke, Brugel, & Mundt 1986; Böhm & Solf 1994). It is reasonable that the shell axis is nearly parallel to that of the outflow. In addition to the outflowing shells, a significant amount of the ambient gas component missed in the NMA observations is expected to exist around T Tauri, as shown in the maps obtained with the 45 m telescope.

The proposed model of the biconical outflowing shells can explain quite well the observational results described in the previous section, if the ^{13}CO rings originate from the shells. First, the assumed orientation of the shells relative to the line of sight explains easily why the blueshifted ring is located southwestward (P.A. $\approx 257°$) compared with the redshifted one on the plane of the sky. Second, the reflection nebula NGC 1555 is observed along the inner edge of the blueshifted ring (see Fig. 4*a*) because the inner surface of the blueshifted shell, which is at the near side, reflects the light of T Tauri. Finally, the fact that the blueshifted and redshifted CO outflows are located inside the blue and red ^{13}CO rings, respectively (see Fig. 5) is understood naturally if we interpret the ^{13}CO rings as the projection on the sky of the swept-up shells outflowing with lower velocities and surrounding the higher velocity components of the outflow, though Schuster et al. (1996) explain their ^{12}CO ($J = 3$–2) outflow maps in a different way. The situation that the higher velocity components of the outflow are surrounded by dense gas with lower velocities has been found commonly in other molecular outflows, for example, in the cases of L1551–IRS 5 (Uchida et al. 1987; Moriarty-Schieven & Snell 1988) and Mon R2 (Xie, Goldsmith, & Patel 1993). We will discuss in detail the driving mechanism and the three-dimensional structure of the outflowing shells in later subsections.

The existence of an infalling envelope with a spatial extent exceeding 1000 AU around T Tauri was suggested in some previous studies (e.g., CHKW; Weintraub et al. 1992; van Langevelde, van Dishoeck, & Blake 1994a). The positional difference between the two ^{13}CO rings could be explained in terms of the infalling shell whose axis inclines northeastward on its near side. It should be noted, however, that such an infalling model is incompatible with the relation between the ^{13}CO rings and the reflection nebula NGC 1555, and with the relation between the ^{13}CO rings and the moderately high velocity outflow; if the axis of the shell would incline northeastward on its near side, the reflection nebula should correspond to the inner edge of the red ring, and the red and blue lobes of the CO outflow should be surrounded by the blue and red rings, respectively, contrary to the observed structure. Our outflowing shell model is consistent with the observed structure.

Some parts of the ^{13}CO rings seem to be missing in the maps with the NMA observations, i.e., the northern part of the red ring and the southern part of the blue ring (see Figs. 2a–2b). These cases of missing emission may be attributed to the north(red)–south(blue) poorly-collimated outflow system associated with T Tauri, which was found by Solf, Böhm, & Raga (1988) (see also Böhm & Solf 1994). The physical nature of this outflow system is not so clear, because there are no similar outflow systems in the cases of other T Tauri stars (Böhm & Solf 1994). Nevertheless, an image of the H_2 emission line at $\lambda = 2$ μm shows a structure elongated in the north-south direction (van Langevelde et al. 1994b), suggesting that the north-south outflow system is so energetic as to excite H_2 molecules by collisional heating. Such a poorly collimated energetic ouflow may break the shells if the axis of this outflow system deviates from that of the shells; i.e., the northern red lobe of the north-south outflow may have blown away the northern part of the redshifted outflowing shells, while the southern blue lobe may have blown off the southern part of the blueshifted outflowing shells.

On the other hand, the origin of the spatially compact features at 3″ east of T Tauri at all the blueshifted velocities and 7″ southwest of T Tauri at the velocities redshifted by more than 1 km s^{-1} is less certain. The velocity gradient in the east(blue)–west(red) direction cannot be explained by either Keplerian rotation or infall in a disklike structure if the axis of the disk is identical with that of the outflowing shells. Moreover, the line-of-sight velocities of the compact features are inconsistent with the velocities expected from either rotation or infall in the disklike structure, as shown below. The maximum line-of-sight velocity of the gas expected for Keplerian rotation is

$$0.62\left(\frac{M_*}{2\,M_\odot}\right)^{1/2}\left(\frac{\sin i}{\sin 10°}\right)\left(\frac{s}{1''}\right)^{-1/2}\ \text{km s}^{-1}, \qquad (2)$$

and that expected for disklike infall is

$$0.87\left(\frac{M_*}{2\,M_\odot}\right)^{1/2}\left(\frac{\sin i \cos^{1/2} i}{\sin 10° \cos^{1/2} 10°}\right)\left(\frac{s}{1''}\right)^{-1/2}\ \text{km s}^{-1}, \qquad (3)$$

where s is the angular separation from T Tauri and i is the angle between the disk axis and the line of sight. The observed line-of-sight velocities for the compact features (blueshifted by 0.13–2.35 km s^{-1} at 3″ east and redshifted by 1.05–1.47 km s^{-1} at 7″ southwest of T Tauri) exceed the values obtained from equations (2) and (3). If the emission originates from an axisymmetric infalling envelope with bipolar cavities, the line-of-sight velocity can be larger than equation (3) and comparable to the observed velocities. In this case, however, it is difficult to explain the observed velocity gradient along the east-west direction because each of the blueshifted and redshifted components must be observed both east and west of T Tauri.

It is most plausible that these compact features originate from an outflowing gas that is on the surface of the geometrically thick disk around T Tauri, as shown in Figure 8. In the eastern half of the disk, the outflowing gas on the nearer surface is observed as the blueshifted compact feature, while the outflowing gas on the farther surface is hardly observed with the NMA because the components whose line-of-sight velocities are close to the systemic velocity are easily resolved out. Similarly, in the western half of the disk, we can observe only the gas on the farther surface of the disk as the redshifted compact feature. The reflection nebula in the vicinity of T Tauri discovered by Nakajima & Golimowski (1995) is well understood in terms of the scattered light from the surface of this geometrically thisk disk. A similar outflowing gas with a disklike structure has also been found around DG Tauri by Kitamura, Kawabe, & Saito (1996).

© American Astronomical Society • Provided by the NASA Astrophysics Data System

1996ApJ...470.1001M

4.2. *Physical Nature of the Outflowing Shells*

4.2.1. *The Dynamical Timescale of the Shells*

We can identify six emission peaks designated A through F in the position-velocity (P-V) diagram along a line passing through T Tauri at P.A. = 77° (Fig. 3). As shown in the Appendix with a simplified model, we can obtain some restriction on the dynamical timescale of each emission peak from its projected distance from the star and line-of-sight velocity. From these restrictions, we find that the dynamical timescale of the shell, $\tau_{\rm dyn}$, should satisfy

$$2.5 \times 10^4 \text{ yr} < \tau_{\rm dyn} < 7.3 \times 10^4 \text{ yr} . \quad (4)$$

4.2.2. *The Driving Source of the Outflowing Shells*

It is accepted in general that the molecular outflows associated with low-mass young stellar objects are driven by the neutral components of winds or jets with extremely high velocities (≥ 100 km s^{-1}) (e.g., Lizano et al. 1988; Koo 1989). These extremely high velocity winds or jets (EHVs) are probably ejected from just the vicinity of stellar surfaces (see, e.g., Shu et al. 1994). Around T Tauri, the H I emission from EHVs has been marginally detected (Ruiz, Alonso, & Mirabel 1992). Ruiz et al. (1992) have estimated the physical quantities of the EHVs and have concluded that the EHVs can drive the molecular outflow associated with T Tauri. It would be natural to imagine that the outflowing shells are also driven by the EHVs. In order to examine this idea, we shall compare the momentum supply rate of EHVs with the momentum supply rates to the outflowing shells.

The momenta along the line of sight of the blueshifted and redshifted outflowing shells, $P_{\rm blue}$ and $P_{\rm red}$, are expressed as

$$P_{\rm blue} = \sum_{v_r < v_{\rm sys}} M(v_r) \, | v_r - v_{\rm sys} | , \quad (5a)$$

$$P_{\rm red} = \sum_{v_r > v_{\rm sys}} M(v_r) \, | v_r - v_{\rm sys} | , \quad (5b)$$

where $v_{\rm sys}$ is the systemic velocity and $M(v_r)$ is the gas mass in each radial velocity range. Assuming the optically thin ^{13}CO emission, $T_{\rm ex} = 10$–30 K, and $X(^{13}{\rm CO}) = (1$–$2) \times 10^{-6}$ in calculating $M(v_r)$ according to equation (1), we obtain

$$P_{\rm blue} = (0.033\text{–}0.14) \, M_\odot \text{ km s}^{-1} , \quad (6a)$$

$$P_{\rm red} = (0.006\text{–}0.026) \, M_\odot \text{ km s}^{-1} . \quad (6b)$$

By taking the dynamical timescale of the shells $\tau_{\rm dyn} = 5 \times 10^4$ yr (see eq. [4]), the momentum supply rates to the blueshifted and redshifted shells are estimated, respectively, to be

$$\dot{P}({\rm shell})_{\rm blue} = P_{\rm blue}/\tau_{\rm dyn} = (6.6\text{–}28) \times 10^{-7} \, M_\odot \text{ km s}^{-1} \text{ yr}^{-1} , \quad (7a)$$

$$\dot{P}({\rm shell})_{\rm red} = P_{\rm red}/\tau_{\rm dyn} = (1.2\text{–}5.2) \times 10^{-7} \, M_\odot \text{ km s}^{-1} \text{ yr}^{-1} . \quad (7b)$$

In Table 1, we summarize $\dot{P}$(shell) given by equations (7a) and (7b), the momentum supply rates to the extended molecular outflow, $\dot{P}$(outflow), derived from Levreault's (1988) observations, and the momentum supply rate by the EHVs, $\dot{P}$(EHV), obtained by Ruiz et al. (1992). In principle, we can judge whether the EHVs can drive the shells or not by comparing $\dot{P}$(EHV) with $\dot{P}$(shell). However, $\dot{P}$(EHV) estimated by Ruiz et al. (1992) is less certain, because the spatial extent of the EHVs was not directly obtained from their observations. On the other hand, $\dot{P}$(outflow) would give a lower limit to $\dot{P}$(EHV) because the molecular outflow around T Tauri must be driven by the EHVs ejected from T Tauri as in the cases of the other outflow sources (e.g., Lizano et al. 1988; Koo 1989). Hence, the comparison of $\dot{P}$(shell) with $\dot{P}$(outflow) would give some information on whether the EHVs can be the driving source of the shells.

Table 1 shows that values of $\dot{P}({\rm outflow})_{\rm blue/red}$ are larger than $\dot{P}({\rm shell})_{\rm blue/red}$ by an order of magnitude. Because of the uncertainty in $\tau_{\rm dyn}$ as seen in equation (4), $\dot{P}$(shell) in Table 1 has an uncertainty of a factor of ~ 2. Even if we take into account the fact that emission components of lower spatial frequencies are missing in the aperture synthesis observations, $\dot{P}$(shell) can hardly be underestimated by more than a factor of 10. This is because the NMA observations resolved out the emission mainly in the velocity range of $| v_r - v_{\rm sys} | < 0.5$ km s^{-1}, in which the ambient cloud emission predominates rather than that of the outflowing shells, as described in § 3.2 (see Fig. 7). Therefore, we can conclude that the EHVs are energetic enough to drive the outflowing shells around T Tauri.

4.2.3. *Three-dimensional Structure of the Shells: Dispersal of the Parent Cloud Core*

In the Appendix we estimate the distance D_p of the emission peak p (p for A through F in Fig. 3) from the central star and its angular position ϕ_p measured from the axis of the shells (by definition $0° < \phi_p < 90°$). Because of the uncertainty in $\tau_{\rm dyn}$ as shown in equation (4), we can determine only the maximum and minimum values of ϕ_p and D_p. The results are shown in columns (2) through (5) of Table 2. In addition we list ϕ_p and D_p for the case of $\tau_{\rm dyn} = 5 \times 10^4$ yr in columns (6) and (7). As seen from Table 2, the estimated values of ϕ_p and D_p agree fairly well among the

TABLE 1

MOMENTUM SUPPLY RATES TO THE OUTFLOWING SHELLS AND TO THE MOLECULAR OUTFLOW, AND THE MOMENTUM SUPPLY RATE FROM THE EHVs

Component	$\dot{P}$(Shell)[a] ($M_\odot$ km s^{-1} yr^{-1})	$\dot{P}$(Outflow)[b] ($M_\odot$ km s^{-1} yr^{-1})	$\dot{P}$(EHV)[c] ($M_\odot$ km s^{-1} yr^{-1})
Blue	$(6.6\text{–}28) \times 10^{-7}$	4×10^{-5}	6.6×10^{-5}
Red.....	$(1.2\text{–}5.2) \times 10^{-7}$	7×10^{-6}	...[d]

[a] The dynamical timescale of the shells, $\tau_{\rm dyn} = 5 \times 10^4$ yr, has been adopted.
[b] From Levreault 1988.
[c] From Ruiz et al. 1992.
[d] Cannot be established because of strong contamination by a cloud complex (see Ruiz et al. 1992).

© American Astronomical Society • Provided by the NASA Astrophysics Data System

1996ApJ...470.1001M

TABLE 2

RANGES OF THE DISTANCES AND THE ANGULAR POSITIONS OF THE EMISSION PEAKS

	ϕ_p[a] (deg)		D_p[a] (10^3 AU)		ϕ_p[b]	D_p[b]
p (1)	Minimum (2)	Maximum (3)	Minimum (4)	Maximum (5)	(deg) (6)	(10^3 AU) (7)
A.....	34	61	3.0	4.1	45	3.5
B.....	53	80	2.9	4.0	64	3.4
C.....	35	64	5.1	10	44	7.4
D.....	20	38	3.6	9.7	25	6.7
E.....	16	45	5.6	11	25	8.0
F.....	10	37	7.8	17	18	12

[a] The dynamical timescale of the shells τ_{dyn} is assumed to be between 2.5×10^4 yr and 7.3×10^4 yr (see eq. [4]).
[b] $\tau_{dyn} = 5 \times 10^4$ yr.

redshifted peaks (A though C) and among the blueshifted peaks (D through F) individually.

In Table 3, we list the distances and angular positions averaged among the blushifted emission peaks in Figure 3 ($\bar{D}_{blue}$, $\bar{\phi}_{blue}$; first row), the redshifted peaks ($\bar{D}_{red}$, $\bar{\phi}_{red}$; second row), and all the peaks ($\bar{D}_{all}$ and $\bar{\phi}_{all}$; third row) for the three cases of τ_{dyn} (2.5×10^4, 5×10^4, and 7.3×10^4 yr; see eq. [4]). There are differences of a factor of ~ 2 between $\bar{D}_{blue}$ and $\bar{D}_{red}$ and between $\bar{\phi}_{blue}$ and $\bar{\phi}_{red}$. Such differences are well demonstrated in Figure 9, which shows the positions of all the emission peaks in Figure 3 for the case of $\tau_{dyn} = 5 \times 10^4$ yr (see cols. [6] and [7] of Table 2). These differences may be artifacts caused by the estimation error in the systemic velocity (v_{sys}). For example, if v_{sys} is in fact $+8.0$ km s^{-1} instead of $+8.2$ km s^{-1}, these differences almost disappear, as shown in columns (8) and (9) of Table 3. It is understood easily that ($\bar{D}_{blue}$, $\bar{\phi}_{blue}$) and ($\bar{D}_{red}$, $\bar{\phi}_{red}$) are sensitive to a slight change in the systemic velocity. On the contrary, the values averaged for both blueshifted and redshifted peaks ($\bar{D}_{all}$ and $\bar{\phi}_{all}$) are rather insensitive to the adopted v_{sys} as seen in Table 3 (compare cols. [4] and [5] with cols. [8] and [9], respectively). Thus, we shall use only ($\bar{D}_{all}$, $\bar{\phi}_{all}$) in the following discussion.

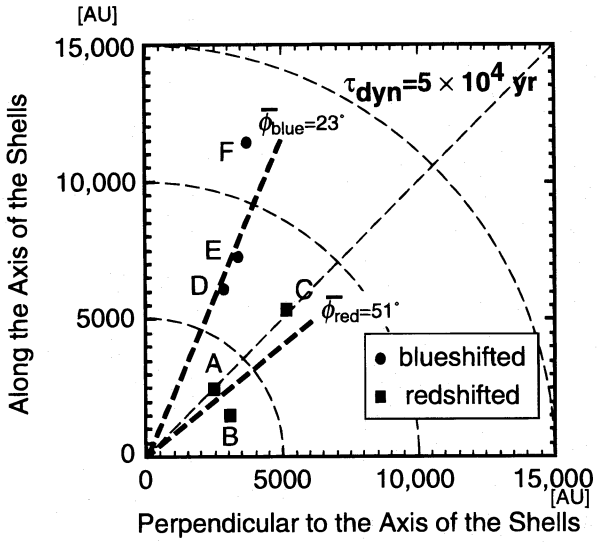

FIG. 9.—Positions of the emission peaks for the case of $\tau_{dyn} = 5 \times 10^4$ yr. All the peaks are plotted according to the absolute values of their coordinates.

It is noteworthy that the possible range of $\bar{D}_{all}$, 4.7×10^3 AU to 9.3×10^3 AU (Table 3), is nearly equal to or slightly smaller than 10^4 AU, which is the typical radius of molecular cloud cores in the Taurus Molecular Cloud (Myers & Benson 1983). This fact implies that the pair of the outflowing shells is a part of the remaining cloud core around T Tauri. Moreover, the shells have the outflowing motion probably driven by the high-velocity stellar wind as discussed in § 4.2.2. Therefore, it can be concluded that a part of the molecular cloud core around T Tauri is now dispersing under the influence of the high-velocity wind ejected from T Tauri. Such a dispersing process will stop the growth of the central star and fix the mass of the forming star as investigated by Nakano, Hasegawa, & Norman (1995).

The averaged opening angle of all the emission peaks, $\bar{\phi}_{all}$, lies between 28° and 54° (see Table 3); most of the parent cloud core at $\phi < \bar{\phi}_{all}$ must have been blown off by the EHVs. Whitney & Hartmann (1993) calculated the images of scattered near-IR radiation employing model envelopes around young stellar objects. Comparing their model calculations with the near-IR observations of T

TABLE 3

THE MEAN DISTANCE $\bar{D}$ (IN 10^3 AU) AND THE MEAN ANGULAR POSITION $\bar{\phi}$ (IN DEGREES) OF THE EMISSION PEAKS FOR SOME VALUES OF τ_{dyn}

	$\tau_{dyn} = 2.5 \times 10^4$ yr[a]		$\tau_{dyn} = 5.0 \times 10^4$ yr[a]		$\tau_{dyn} = 7.3 \times 10^4$ yr[a]		$\tau_{dyn} = 5.0 \times 10^4$ yr[b]	
PEAKS (1)	$\bar{D}$ (2)	$\bar{\phi}$ (3)	$\bar{D}$ (4)	$\bar{\phi}$ (5)	$\bar{D}$ (6)	$\bar{\phi}$ (7)	$\bar{D}$ (8)	$\bar{\phi}$ (9)
Blue.....	5.7	40	8.9	23	13	15	7.5	29
Red	3.7	71	4.8	51	6.0	41	6.5	34
All	4.7	54	6.8	37	9.3	28	7.1	32

[a] The systemic velocity of T Tauri, $V_{LSR} = +8.2$ km s^{-1}, has been adopted.
[b] The systemic velocity of T Tauri, $V_{LSR} = +8.0$ km s^{-1}, has been adopted.

© American Astronomical Society • Provided by the NASA Astrophysics Data System

1996ApJ...470.1001M

Tauri (Weintraub et al. 1992), they found that the most plausible model is an envelope having parabolic holes with an opening angle of $\sim 30°$ at large radii. According to CHKW, the envelope model that can reproduce the SED of T Tauri also requires a bipolar cavity with an opening angle of 20°, which is somewhat smaller than our estimation. In summary, the values of $\bar{\phi}_{\rm all}$ we have obtained are in good agreement with those obtained in the previous studies.

4.3. *Evolutionary Stage of T Tauri and Unresolved Problems*

Myers et al. (1987) (see also Beichmanet al. 1986) have shown that class I sources tend to exist at the centers of ammonia cores, suggesting that these sources are deeply embedded within dense cloud cores with spatial extent of $\sim 10^4$ AU and that they are good candidates for mass accreting protostars. On the other hand, recent observations with high spatial resolutions at millimeter wavelengths have revealed that typical class II sources (i.e., T Tauri stars) are accompanied by compact gaseous disks with radius smaller than 10^3 AU, which often show Keplerian rotation, instead of spatially extended gaseous structures. The latter category includes GG Tauri (Kawabe et al. 1993; Dutrey, Guilloteau, & Simon 1994), GM Aurigae (Koerner, Sargent, & Beckwith 1993), DM Tauri (Saito et al. 1995), and four other T Tauri stars (Koerner & Sargent 1995). It is now widely accepted that class I (or optically invisible) sources evolve into class II (or optically visible) sources as a result of dissipation of their envelopes (Beichman et al. 1986; Adams et al. 1987; Myers et al. 1987; Hayashi et al. 1994).

With this scenario of the evolution, one can naturally expect that there is a transitional phase between class I and class II sources in which a central source is associated with a spatially extended and dispersing envelope. The present observations suggest that T Tauri is a source in this transitional phase. It must be noted that the environment around T Tauri is quite different from those around both class I and class II sources. Class I sources are usually at or near the emission peaks of spatially extended cloud cores even if they are observed with a high angular resolution (e.g., Ohashi et al. 1996), while T Tauri is not located at a peak of the well-defined cloud core. On the other hand, T Tauri is associated with a more extended gaseous structure compared with the typical class II sources like GG Tauri or DM Tauri. Such differences in environment may be due to an evolutional effect, i.e., T Tauri is older than class I sources but much younger than typical class II sources. This is consistent with our suggestion that T Tauri is in the transitional phase from a protostar to a typical T Tauri star.

In the Taurus Molecular Cloud, there are two other T Tauri stars that exhibit the characteristics expected for the transitional phase. One is HL Tauri, around which dynamical mass accretion onto the central star-disk system is still going on (Hayashi et al. 1993; Lin et al. 1994; see also Cabrit et al. 1996). The other is DG Tauri, which is accompanied by a "dispersing gaseous disk" with a radius of 2000 AU (Kitamura et al. 1996), suggesting that the remnant of the parent core is being blown off by the stellar wind as in the case of T Tauri. It is remarkable that all three T Tauri stars (T Tauri, HL Tauri, and DG Tauri) show flat SEDs with significant luminosity excesses at IR wavelengths. These observational facts may imply that the flat spectrum T Tauri stars are accompanied by spatially extended gaseous structures and are in the transitional phase from protostars to typical T Tauri stars.

One of the unresolved problems is whether infalling gas exists around T Tauri or not. Although the existence of the infalling envelope around T Tauri was suggested by some previous studies (Weintraub et al. 1992; Whitney & Hartmann 1993; CHKW; van Langevelde et al. 1994a), no direct evidence has been obtained in the present observations. Recent theoretical studies have shown that infalling envelopes around young stellar objects are expected to have disklike structures like that around HL Tauri (e.g., Galli & Shu 1993a, 1993b; Hartmann et al. 1994; Nakamura, Hanawa, & Nakano 1995). An infalling gaseous disk around T Tauri, even if it exists, would hardly be detected because of its nearly pole-on configuration (e.g., Herbst et al. 1986); the infalling gas in a disklike structure in a pole-on configuration is expected to have so small line-of-sight velocities that it is contaminated severely by the ambient molecular cloud. Further observations with higher velocity resolutions are required for settling this problem.

Another unresolved problem is the slight discrepancy in the opening angle of the shells between our estimation (37° if $\tau_{\rm dyn} = 5 \times 10^4$ yr) and that from the model constructed by CHKW (20°). CHKW discussed that if the opening angle of the shells is larger, the flux densities at mid- to far-infrared wavelengths become smaller than the observed ones because of the lack of dust with high temperatures (see Fig. 6 in CHKW). If the larger opening angle estimated from our observations is real, CHKW's discussion may suggest the existence of an additional source for mid-to far-infrared emission, e.g., a circumstellar disk with shallower radial gradient of the temperature (Adams et al. 1988) or the IR companion T Tau(S), whose contribution to the emission at wavelengths longer than 20 μm has not been evaluated (see Ghez et al. 1991; Maihara & Kataza 1991).

5. CONCLUSIONS

We have made aperture synthesis observations of T Tauri with the Nobeyama Millimeter Array (NMA) and mapping observations around T Tauri with the Nobeyama 45 m telescope with the ^{13}CO ($J = 1$–0) line. Our main results are summarized as follows:

1. We have found from the NMA observations a pair of ringlike ^{13}CO ($J = 1$–0) emissions with a radius of $\sim 30''$, corresponding to ~ 4200 AU at the distance 140 pc to T Tauri, detected at velocities blueshifted or redshifted by ~ 1 km s^{-1} from the systemic velocity. In addition to these ringlike features, two compact features have been detected in the vicinity of T Tauri. The total mass of the molecular gas detected with the NMA is estimated to be 0.054–0.23 $M_\odot$ with the assumption of the optically thin ^{13}CO emission.

2. The maps obtained by the 45 m telescope show a smoothly extended feature near the systemic velocity, as well as the ringlike and compact features detected with the NMA. The total mass of the gas detected by the 45 m telescope is estimated to be 0.31–1.3 $M_\odot$ under the same assumption used for the NMA results. The difference in the estimated mass between the NMA and 45 m observations is mainly due to resolving out of the smoothly extended feature in the NMA observations.

3. The reflection nebula NGC 1555 associated with T Tauri well delineates the inner edge of the blueshifted ^{13}CO ring. Moreover, the ^{13}CO rings surround the moderately high velocity outflow. Such characteristics of the ^{13}CO

© American Astronomical Society • Provided by the NASA Astrophysics Data System

1996ApJ...470.1001M

rings as well as their morphology and velocity field can be well explained with a model of biconical outflowing shells in a nearly pole-on configuration.

4. The momentum supply rate of the stellar wind ejected from T Tauri is estimated to be much higher than the momentum supply rate to the outflowing shells. This suggests that the outflowing shells are driven by the high-velocity stellar wind.

5. We estimated the three-dimensional structure of the outflowing shells by correcting for the projection effect on the plane of the sky, and we found that the spatial extent of the shells is nearly equal to or slightly smaller than the typical size of the molecular cloud cores ($\sim 10^4$ AU in radius) in the Taurus Molecular Cloud. This indicates that the biconical outflowing shells are part of the parent cloud core around T Tauri, which is dispersing under the influence of the stellar wind.

6. The environment around T Tauri shown in the present observations is quite different from those around typical T Tauri stars in which central sources are associated with compact gaseous components. According to the widely accepted scenario in which embedded protostars evolve into optically visible T Tauri stars as a result of dissipation of their envelopes, the above difference in the environment is understood naturally as the difference in the evolutional phase, i.e., T Tauri is much younger than the other typical T Tauri stars and is in the transitional phase from a protostar to a typical T Tauri star.

7. We did not find any infalling gas around T Tauri in the present observations, although the existence of the infalling envelope around T Tauri has been predicted by some previous studies. It might be possible that the infalling gas is contaminated severely by the ambient molecular cloud if the infalling gas is confined to a disklike structure in a pole-on configuration to us.

We thank the staff members of the Nobeyama Radio Observatory for their help during our observations. We are grateful to K. Hodapp, K. Schuster, and T. Nakajima for kindly supplying their images of T Tauri. We also thank L. Hartmann for his valuable comments and the anonymous referee for helpful suggestions to improve the paper. N. O. is supported by a Smithsonian Postdoctoral Fellowship.

APPENDIX

THE DYNAMICAL TIMESCALE AND THE THREE-DIMENSIONAL STRUCTURE OF THE SHELLS

We estimate the dynamical timescale and three-dimensional structure of the outflowing shells by using positions and velocities of the six emission peaks A through F in the shell features seen in the position-velocity (P-V) diagram at P.A. = 77° (Fig. 10a).

For simplicity, we adopt a model presented in Figure 10b. In this model, we suppose that the angle i between the axis of the shells and the line of sight is 10°, and that the gas in the shells is moving radially from the star. We assume also that the emission peaks are outside the cones with an opening angle of 10° and are more than 10° above or below the equatorial plane, which is perpendicular to the axis of the shells (the shaded area in Fig. 10*b*). It is found that the latter angle is a reasonable lower limit to the actual angle between the outflowing gas and the equatorial plane from the following estimation. A Keplerian disk in equilibrium has an effective half-thickness H given by $H/R \approx 2^{1/2} C_s/V_K$, where R is the distance from the central star, C_s is the isothermal sound velocity, and V_K is the Keplerian orbital velocity. For the mass of the central star $M_* = 2\ M_\odot$, $R = 10^3$ AU, and even a temperature as low as 10 K, we have $H/R \approx 0.20$, which corresponds to an angle of 11° to the star. We have even higher H/R for larger R. Thus, the restriction we have placed on the positions of the emission peaks is not too strict. The positions of the emission peaks are specified by their radial distances from the star (e.g., D_A for peak A) and their angular positions measured from the axis of the shells (e.g., ϕ_A for A) (see Fig. 9*b*). For this model, ϕ_p (p: A through F) must be between 10° and 80°.

We estimate the dynamical timescale of the outflowing shells, τ_{dyn}, in the following way. First we define the dynamical timescale τ_p for each emission peak as

$$\tau_p = \frac{D_p}{V_p}\,, \tag{A1}$$

where V_p is the outflowing velocity of peak p. D_p and V_p are related to the two observed quantities, the projected distance from the star, d_p, and the line-of-sight velocity v_p, as follows (see Fig. 10*b*):

$$D_p = \frac{d_p}{\sin\,(\phi_p \pm i)}\,, \tag{A2a}$$

$$V_p = \frac{v_p}{\cos\,(\phi_p \pm i)}\,, \tag{A2b}$$

where the plus sign is for p = A, E, and F, and the minus sign for p = B, C, and D. Equations (A1) and (A2) give

$$\tau_p = \frac{d_p}{v_p \tan\,(\phi_p \pm i)}\,. \tag{A3}$$

From the assumptions that $i = 10°$ and $10° < \phi_p < 80°$, we obtain upper or lower limits to τ_p:

$$\tau_p < \frac{d_p}{v_p \tan 20°} \quad \text{for } p = \text{A, E, and F}\,, \tag{A4a}$$

© American Astronomical Society • Provided by the NASA Astrophysics Data System

1996ApJ...470.1001M

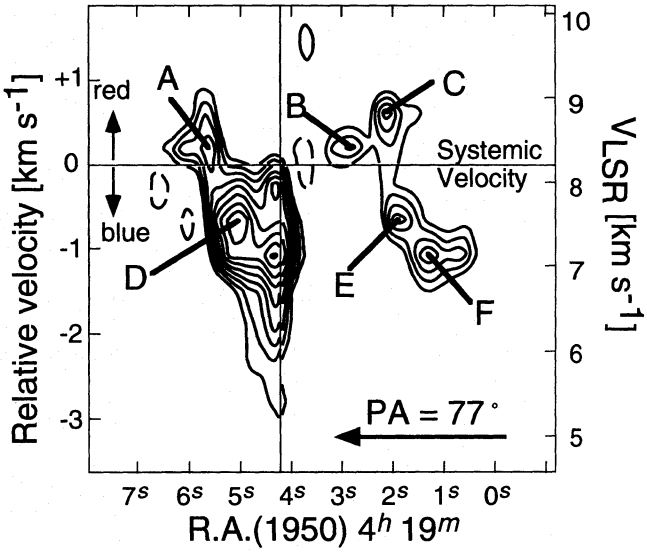

FIG. 10*a*

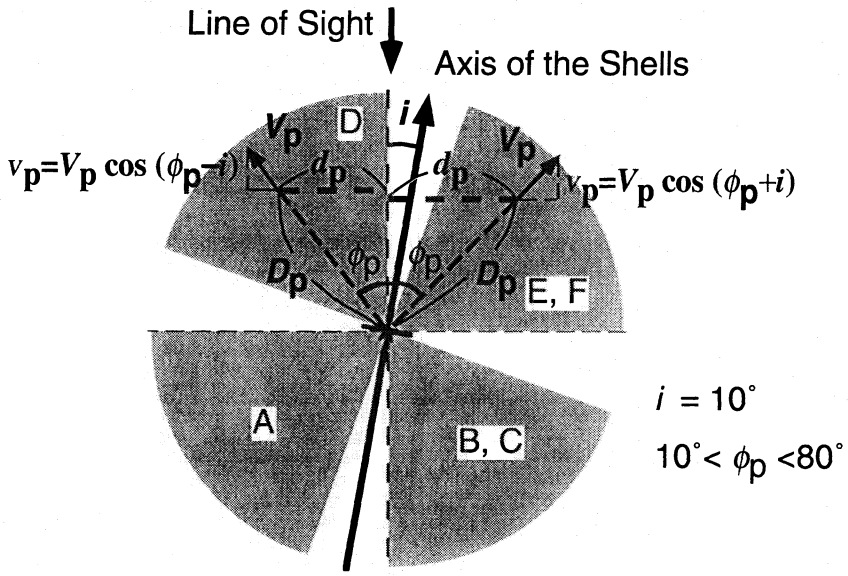

FIG. 10*b*

FIG. 10.—(*a*) Position-velocity diagram at P.A. = 77°, the same as in Fig. 3. Six peaks of the emission contained in the shell features are marked by the letters A–F. (*b*) A model for estimating the dynamical timescale and the three-dimensional structure of the shells. We assume that each emission peak in (*a*) is in one of the shaded areas and is moving radially from the star. Each letter identifies the area to which the emission peak belongs.

$$\tau_p > \frac{d_p}{v_p \tan 70^\circ} \quad \text{for } p = \text{B, C, and D} . \tag{A4b}$$

Table 4 shows the restrictions on τ_p derived from equation (A4a) or (A4b) together with d_p and v_p. Assuming that all the emission peaks have the same dynamical timescale, τ_{dyn}, we can estimate the possible range of τ_{dyn} in such a way that τ_{dyn} should satisfy all the restrictions on τ_p, as

$$2.5 \times 10^4 \text{ yr} < \tau_{dyn} < 7.3 \times 10^4 \text{ yr} . \tag{A5}$$

For the allowable range of τ_{dyn} given by equation (A5), we can derive from equation (A3) the range of ϕ_p for the emission peak p (p: A through F) as

$$\arctan \frac{d_p}{v_p \max(\tau_{dyn})} \pm i < \phi_p < \arctan \frac{d_p}{v_p \min(\tau_{dyn})} \pm i , \tag{A6}$$

where $i = 10^\circ$, $\max(\tau_{dyn}) = 7.3 \times 10^4$ yr, $\min(\tau_{dyn}) = 2.5 \times 10^4$ yr, the minus sign is for p = A, E, and F, and the plus sign for p = B, C, and D.

© American Astronomical Society • Provided by the NASA Astrophysics Data System

1996ApJ...470.1001M

TABLE 4

RESTRICTIONS ON THE DYNAMICAL TIMESCALE τ_p FOR EACH EMISSION PEAK

p	d_p[a] (10^3 AU)	v_p[b] (km s^{-1})	τ_p (10^4 yr)
A.....	2.8	+0.20	<19
B.....	2.7	+0.20	>2.5
C.....	4.1	+0.62	>1.2
D.....	1.7	−0.65	>0.47
E.....	4.6	−0.65	<9.7
F.....	5.8	−1.08	<7.3

[a] A distance to T Tauri of 140 pc has been adopted.

[b] A systemic velocity of T Tauri, $V_{LSR} = +8.2$ km s^{-1}, has been adopted.

We can also derive from equation (A2a) the range of D_p as

$$\frac{d_p}{\sin\,[\max\,(\phi_p) \pm i]} < D_p < \frac{d_p}{\sin\,[\min\,(\phi_p) \pm i]}\,, \tag{A7}$$

where min (ϕ_p) and max (ϕ_p) are, respectively, the minimum and the maximum values of ϕ_p obtained from equation (A6), the plus sign is for p = A, E, and F, and the minus sign for p = B, C, and D.

Columns (2) through (5) of Table 2 show the minimum and maximum values of ϕ_p and D_p derived from equations (A6) and (A7) for all the emission peaks. In addition, ϕ_p and D_p for the case of $\tau_{dyn} = 5 \times 10^4$ yr are listed in columns (6) and (7). As seen from Table 2, the estimated values of ϕ_p and D_p agree fairly well among the redshifted peaks (A through C) and among the blueshifted peaks (D through F) individually. This agreement suggests that our simple three-dimensional model is physically reasonable.

REFERENCES

Adams, F. C., Lada, C. J., & Shu, F. H. 1987, ApJ, 312, 788
———. 1988, ApJ, 326, 865
Adams, F. C., & Shu, F. H. 1986, ApJ, 308, 836
Beichman, C. A., Myers, P. C., Emerson, J. P., Harris, S., Benson, P. J., & Jennings, R. E. 1986, ApJ, 307, 337
Bertout, C., Basri, G., & Bouvier, J. 1988, ApJ, 330, 350
Böhm, K. H., & Solf, J. 1994, ApJ, 430, 277
Bührke, T., Brugel, E. W., & Mundt, R. 1986, A&A, 163, 83
Cabrit, S., Guilloteau, S., André, P., Bertout, C., Montmerle, T., & Schuster, K. 1996, A&A, 305, 527
Calvet, N., Hartmann, L., Kenyon, S. J., & Whitney, B. A. 1994, ApJ, 434, 330 (CHKW)
Chikada, Y., et al. 1987, Proc. IEEE, 75, 1203
Dutrey, A., Guilloteau, S., & Simon, M. 1994, A&A, 286, 149
Dyck, H. M., Simon, T., & Zuckerman, B. 1982, ApJ, 255, L103
Edwards, S., & Snell, R. L. 1982, ApJ, 261, 151
Elias, J. H. 1978, ApJ, 224, 857
Galli, D., & Shu, F. H. 1993a, ApJ, 417, 220
———. 1993b, ApJ, 417, 243
Ghez, A. M., et al. 1991, AJ, 102, 2066
Hartmann, L., Boss, A., Calvet, N., & Whitney, B. 1994, ApJ, 430, L49
Hartmann, L., Hewett, R., Stahler, S., & Mathieu, R. 1986, ApJ, 309, 275
Hayashi, M., Hasegawa, T., Ohashi, N., & Sunada, K. 1994, ApJ, 426, 234
Hayashi, M., Ohashi, N., & Miyama, S. M. 1993, ApJ, 418, L71
Herbig, G. H., & Bell, K. R. 1988, Lick Obs. Bull., No. 1111
Herbst, W., et al. 1986, ApJ, 310, L71
Hodapp, K. W. 1994, ApJS, 94, 615
Kawabe, R., Ishiguro, M., Omodaka, T., Kitamura, Y., & Miyama, S. M. 1993, ApJ, 404, L63
Kenyon, S. J., Calvet, N., & Hartmann, L. 1993, ApJ, 414, 676
Kenyon, S. J., & Hartmann, L. 1987, ApJ, 323, 714
Kitamura, Y., Kawabe, R., & Saito, M. 1996, ApJ, 457, 277
Koerner, D. W., & Sargent, A. I. 1995, AJ, 109, 2138
Koerner, D. W., Sargent, A. I., & Beckwith, S. V. W. 1993, Icarus, 106, 2
Koo, B.-C. 1989, ApJ, 337, 318
Kutner, M. L., & Ulich, B. L. 1981, ApJ, 250, 341
Lada, C. J. 1987, in IAU Symp. 115, Star Forming Regions, ed. M. Peimbert & J. Jugaku (Dordrecht: Reidel), 1
Lada, C. J., & Wilking, B. A. 1984, ApJ, 287, 610
Levreault, R. M. 1988, ApJS, 67, 283
Lin, D. N. C., Hayashi, M., Bell, K. R., & Ohashi, N. 1994, ApJ, 435, 821
Lizano, S., et al. 1988, ApJ, 328, 763
Maihara, T., & Kataza, H. 1991, A&A, 249, 392
Miyake, K., & Nakagawa, Y. 1995, ApJ, 441, 361
Moriarty-Schieven, G. H., & Snell, R. L. 1988, ApJ, 332, 364
Myers, P. C., & Benson, P. J. 1983, ApJ, 266, 309
Myers, P. C., Fuller, G. A., Mathieu, R. D., Beichman, C. A., Benson, P. J., & Schild, R. E. 1987, ApJ, 319, 340
Nakajima, T., & Golimowski, D. A. 1995, AJ, 109, 1181
Nakamura, F., Hanawa, T., & Nakano, T. 1995, ApJ, 444, 770
Nakano, T., Hasegawa, T., & Norman, C. 1995, ApJ, 450, 183
Ohashi, N., Hayashi, M., Kawabe, R., & Ishiguro, M. 1996, ApJ, in press
Ohashi, N., Kawabe, R., Hayashi, M., & Ishiguro, M. 1991, AJ, 102, 2054
Panagia, N. 1991, in The Physics of Star Formation and Early Stellar Evolution, ed. C. J. Lada & N. D. Kylafis (Dordrecht: Kluwer), 565
Panagia, N., & Felli, M. 1975, A&A, 39, 1
Ruiz, A., Alonso, J. L., & Mirabel, I. F. 1992, ApJ, 394, L57
Saito, M., et al. 1995, ApJ, 453, 384
Schuster, K. H. 1994, Ph.D. thesis, Max-Planck-Institut für Extraterrestrische Physik
Schuster, K. H., Harris, A. I., Anderson, N., & Russell, A. 1993, ApJ, 412, L67
Schuster, K. H., Harris, A. I., Russell, A. P. G., & Genzel, R. 1996, in preparation
Scoville, N. Z., Sargent, A. I., Sanders, D. B., Claussen, M. J., Masson, C. R., Lo, K. Y., & Phillips, T. G. 1986, ApJ, 303, 416
Shu, F. H., Najita, J., Ostriker, E., Wilkin, F., Ruden, S., & Lizano, S. 1994, ApJ, 429, 781
Skinner, S. L., & Brown, A. 1994, AJ, 107, 1461
Solf, J., Böhm, K. H., & Raga, A. 1988, ApJ, 334, 229
Stapelfeldt, K. R., et al. 1995, ApJ, 449, 883
Sunada, K., Kawabe, R., & Inatani, J. 1993, Int. J. Infrared Millimeter Waves, 14, 1251
Sunada, K., Noguchi, T., Tsuboi, M., & Inatani, J. 1995, in ASP Conf. Ser., 75, Multi-Feed Systems for Radio Telescopes, ed. D. T. Emerson & J. M. Payne (San Francisco: ASP), 230
Uchida, Y., Kaifu, N., Shibata, K., Hayashi, S. S., Hasegawa, T., & Hamatake, H. 1987, PASJ, 39, 907
van Langevelde, H. J., van Dishoeck, E. F., & Blake, G. A. 1994a, 425, L45
van Langevelde, H. J., van Dishoeck, E. F., van der Werf, P. P., & Blake, G. A. 1994b, A&A, 287, L25
Weintraub, D. A., Kastner, J. H., Zuckerman, B., & Gatley, I. 1992, ApJ, 391, 784
Weintraub, D. A., Masson, C., & Zuckerman, B. 1989, ApJ, 344, 915 (WMZ)
Whitney, B. A., & Hartmann, L. 1993, ApJ, 402, 605
Xie, T., Goldsmith, P. F., & Patel, N. 1993, 419, L33

© American Astronomical Society • Provided by the NASA Astrophysics Data System